DEVELOPMENT OF PRACTICAL DRAG MODEL FOR MULTIROTOR-TYPE UNMANNED AERIAL VEHICLES AND ITS APPLICATION

Daejin Lim[1], Hyeongseok Kim[1], Kwanjung Yee[2]

[1]Dept. of Mechanical and Aerospace Engineering
Seoul National University, Seoul, Republic of Korea
djlim8433@snu.ac.kr / khs931113@snu.ac.kr

[2]Institute of Advanced Aerospace Technology,
Seoul National University, Seoul, Republic of Korea
kjyee@snu.ac.kr

Abstract

Application area of multirotor-type Unmanned Aerial Vehicles have become popular and diverse in recent years. This trend makes it more important to obtain an optimally designed multirotor for a specific mission in the conceptual design phase. To this end, accurate prediction of a forward flight performance is essential, and one of the most influential factors on forward flight performance is drag force induced by the body frame. In this study, a practical drag estimation model for multirotor-type Unmanned Aerial Vehicles is developed for the conceptual design phase. The drag model is developed based on physical geometry of the body frame of the multirotors considering interference effect between the components. Therefore, the developed model is able to estimate a drag force depending on the variation of the multirotor geometry. The model estimates the drag force through regression equations derived from Computational Fluid Dynamics (CFD) analysis, which makes the model fast and accurate. The drag model is eventually embedded in a design optimization framework. For a generic filming mission, an optimization example is presented with comparative analysis depending on whether the drag model is applied or not. The optimization result shows that the significance of the drag coefficient on the design optimization

NOMENCLATURE

A_{max}	Maximum allowable current of ESC [A]
AR	Aspect ratio
α_{inc}	Inclined angle of a supporting rod [deg]
C_D	Drag coefficient
CFD	Computational Fluid Dynamics
D	Diameter [mm]
D_{rotor}	Rotor diameter [in]
ESC	Electric Speed Controller
η_m	Motor efficiency [%]
f	Equivalent Parasite Drag Area [m^2]
h_{centre}	Height of a centre body [mm]
I_d	Drive current [A]
I_m	Motor current [A]
K_v	Motor speed constant
κ_{inf}	Interference factor
L	Length [mm]
N_{cell}	The number of cells in a battery
N_{rotor}	The number of rotors
Ω_{rotor}	Rotational speed of rotor [RPM]
P_{elec}	Electric power per motor [W]
P_{mech}	Mechanical power per motor [W]
p_{rotor}	Rotor pitch [in]
Re	Reynolds number
ρ	Density [kg/m^3]
S_{ref}	Reference area [m^2]
θ_{pitch}	Pitch angle of the vehicle [deg]
V_∞	Freestream velocity [m/s]
W_{total}	Total weight [g]

SUBSCRIPT

centre	Centre body of the frame
LGL	Landing Gear Leg
LGF	Landing Gear Foot
rod	Supporting rod of the frame

1. INTRODUCTION

A multirotor-type configuration is one of the most popular layouts of small-scale Unmanned Aerial Vehicles (UAVs) in civilian area targeting for leisure or commercial objectives. Moreover, due to superiorities of the multirotors in controllability and manufacturability over other UAVs, there are also increasing needs in industrial markets [1]. In light of their popularization, various multirotors have been developed in all around world, and many studies for the analysis and design of multirotors were carried out [2-8]. Despite many researches for advancement of the design methods for multirotors, one common limitation exists. Most of the precedent studies are mainly focused on estimating hovering time of multirotors. Although some of them also considered a forward flight, they didn't make it clear how they estimated the drag

Presented at 45th European Rotorcraft Forum, Warsaw, Poland, 17-20 September, 2019

force acting on a body frame, or they used a constant drag coefficient of a specific vehicle model or nominal value because of lack of data. If a nominal value is applied to drag coefficient, it raises a question which value is appropriate in the design process. The problem is that the drag coefficient is one of the major parameters that affects the performance of the multirotors. Many analysis results provided by different tools such as EMST [3] or eCalc [8] show the endurance reduction up to 50 % depending on the forward flight condition. One study [6] also investigated the effect of drag coefficient on endurance of the multirotors by using several nominal values for the drag coefficient. According to this study, the variation of the drag coefficient results in significant difference in endurance of multirotors. These facts support the importance of the consideration of the drag force acting on the body frame in analysis of multirotor.

As mentioned first, the application area of the multirotors has been diversified and most of the mission include a forward flight. Therefore, it is necessary to estimate the drag force and its effect on flight performance in the analysis and design of the multirotors. Particularly, in the first stage of the design process, conceptual design phase, estimating drag force is much more essential in order to minimize the risk of undesirable results at the next phase and to avoid mission failure.

Unlike full-scale manned rotorcraft and aircraft for which empirical data and models for drag force have been established for decades, drag data for the small-scale multirotors are lacking due to their shorter history. As such, a practical drag model for the multirotors is developed in this study for the sake of application to the performance analysis and the conceptual design phase. The developed drag model estimates drag force induced from a body frame of the multirotors by considering geometric variation. Hence, this model can be an answer to which value of drag coefficient is appropriate.

The contents of this paper are mainly focused on the methodology of the developed drag model. In Section 2, the philosophy and analysis methods of the drag model is described. Then, the accuracy of the developed model is verified by comparing with Computational Fluid Dynamics (CFD) results. Finally, the developed drag model is embedded in conceptual design optimization framework, CLOUDS [2]. Using CLOUDS, an optimization example is presented for a generic mission profile.

2. DRAG ESTIMATION MODEL

2.1. Model outline

The developed drag model is intended to be applied in the conceptual design phase for the small-scale multirotors. The philosophy of this model is that total drag force is equivalent to the sum of each component drag force with consideration of interference effect. This method is inspired by the drag model for external attachments in Digital DATCOM [9]. Therefore, a body frame of the multirotors is broken down into each component. The total drag force is calculated by Eq. (1), where f means Equivalent Parasite Drag Area (EPDA) defined as $f = C_D S_{ref}$. κ_{inf} is a correlation factor for interference effect.

$$(1) \quad Drag = \frac{1}{2}\rho V_\infty^2 f_{total}, \quad where\ f_{total} = \kappa_{inf} \sum f_{component}$$

The drag coefficient of each component for EPDA is obtained through CFD analysis. CFD solver used in this study is ANSYS FLUENT 19.2 version. All calculations were carried out under steady conditions. Governing equations are Reynolds Averaged Navier-Stokes (RANS) equations with k-ω SST turbulence model considering curvature correction [10, 11].

2.2. Geometry and attitude assumptions

For the drag model, here are some assumptions about the frame geometry of the multirotors. Firstly, a body frame has a radial layout which is shown in Figure 1. Even though there exist numerous frame layouts of the multirotors in real life, the most representative layout is the radial structure. Commercially available body frame kits have this radial structure, for example Tarot FY650, DJI S800, DJI S900, and ARRIS M1050. This layout consists of a centre body, motor-supporting rods, and landing gear. The centre body consists of two plates. The supporting rods are evenly distributed depending on the number of rotors. The landing gear shape is T-shape that consists of two cylinders.

Figure 1: Radial layout of a body frame of the multirotors

For the CFD analyses, this radial layout is modelled using simple solid figures. The supporting rods and landing gear are cylindrical tube. The centre body is modelled as a single circular plate because the cavity between two plates is usually stuffed with electronics. Thus, the radial layout can be determined by 8 geometric variables related with the components (Table 1 and Figure 2). An attached angle of the landing gear is set 30° (Figure 3).

Presented at 45th European Rotorcraft Forum, Warsaw, Poland, 17-20 September, 2019

Table 1: Geometric input paramters

Component	Parameter
Supporting rod	D_{rod}, L_{rod}
Centre body	D_{centre}, h_{centre}
Landing gear	D_{LGL}, L_{LGL}, D_{LGF}, L_{LGF}

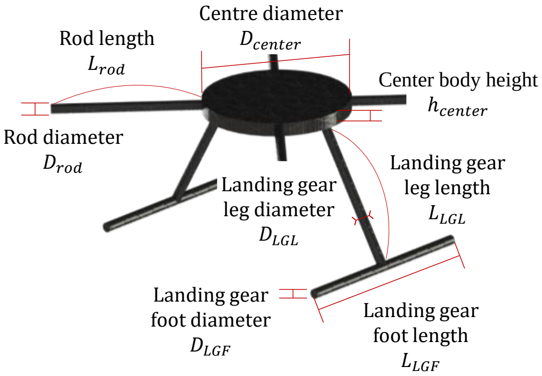

Figure 2: 3D model of the radial layout

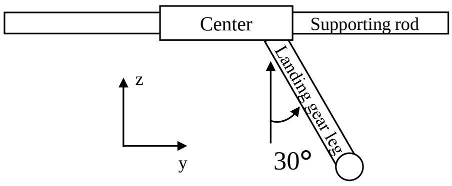

Figure 3: Attached angle of the landing gear

Secondly, flight attitude is assumed to X-position in the forward flight. When the multirotors aviate with X-position in the forward flight, two angles are defined with respect to flow direction: vehicle's pitch angle θ_{pitch} and inclined angle α_{inc}. Their schematics is shown in Figure 4.

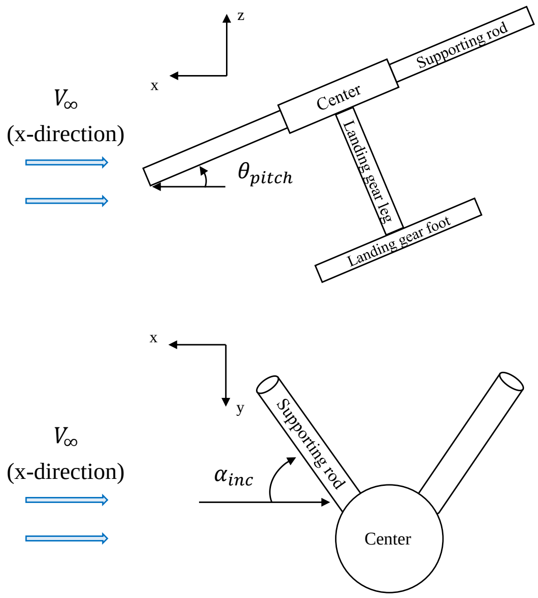

Figure 4: Two angles defined concerning flow direction: vehicle's pitch angle (top) and inclined angle (bottom)

The α_{inc} is settled when the number of rotors is determined because the rotors are evenly distributed. For example, a quadrotor has the inclined angles of 45° and 135°, and a hexarotor has the inclined angles of 30°, 90°, and 150° for each rod.

2.3. Supporting rods (Cylinder)

The supporting rods of the multirotors are modelled as a cylindrical tube, so that CFD analyses were conducted to obtain a drag coefficient of a cylinder. Because the inclined angle has a specific value depending on the number of rotors, the calculation cases were set based on an inclined angle. Figure 5 shows a variation of the drag coefficient of a cylinder by the θ_{pitch}.

(2) $C_{D_{rod}} = f(\theta_{pitch},\ \alpha_{inc}),$

$$where\ S_{ref} = L_{rod} D_{rod}$$

In flight environment where the multirotors generally aviate Reynolds number of a cylinder is between 3,400 and 300,000. In this region called as subcritical region, the drag coefficient of a cylinder remains almost constant, which means that Reynolds number has no effect on the drag coefficient [12]. According to Reference [12], the effect of an Aspect Ratio (AR) can be ignored between 10 and 15 of AR which is a typical value for a supporting rod of the multirotors. The reference geometry information for the calculations is as follows: $D_{rod} = 15\ mm, and\ L_{rod} = 150\ mm$. For the drag model, regression functions are derived based on the CFD analysis results.

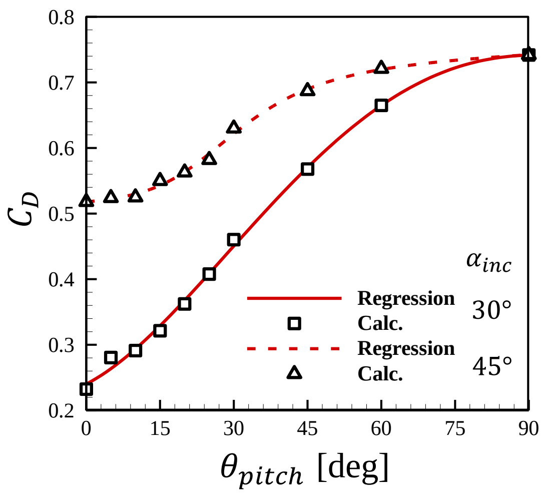

Figure 5: Drag coefficient variation of a cylinder with 10 of AR

Presented at 45th European Rotorcraft Forum, Warsaw, Poland, 17-20 September, 2019

2.4. Centre body (Circular plate)

The centre body is modelled as a circular plate. Unlike the drag coefficient of a cylinder, Reynolds number and AR of a circular plate affect the drag coefficient. Reynolds number effect can be found in Reference [14]. The range of Reynolds number considered here is between 3.40×10^4 and 1.53×10^5. Between these two values, it is assumed that the drag coefficient changes in linear manner. This assumption is based on the fact that the drag coefficient of a flat plate varies in linear manner when the plate is placed parallel to flow direction [14].
As AR of a circular plate increases, the drag coefficient of a circular plate also increases under 45° of the θ_{pitch}. Similar to Reynolds number effect, it is assumed that the drag coefficient changes in linear manner. Reynolds number effect and AR effect is applied independently to each other.

$$(3) \quad C_{D_{centre}} = f(\theta_{pitch}, Re, AR), \quad where\ S_{ref} = \frac{\pi}{4} D_{centre}^2$$

For the drag model, regression functions are derived based on the CFD analysis results.

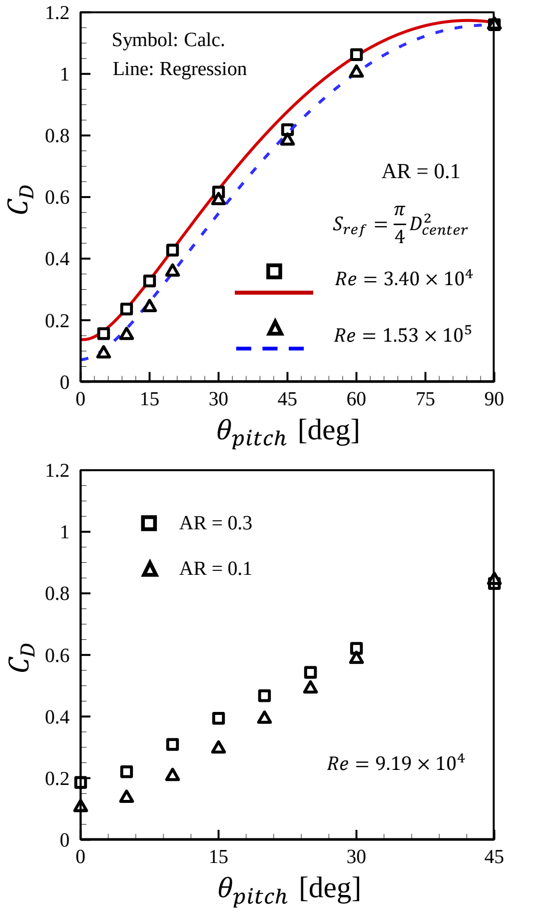

Figure 6: Drag coefficient variation of a circular plate

2.5. Landing gear (Cylinder)

The landing gear is also modelled as a cylindrical tube like the supporting rods. As mentioned in Chapter 2.2, the landing gear has the T-shape configuration which is composed of a leg and foot. The drag coefficient of the landing gear leg can be obtained through the same equation for the supporting rods by the following reasons: 1) The landing gear leg has similar dimension to the supporting rods. 2) The attached angle of the landing gear is 30°. Thus, the equation for the drag coefficient of the landing gear leg is expressed as Eq. (4).

$$(4) \quad C_{D_{LGL}} = f(90 - \theta_{pitch}, \ \alpha_{inc} = 30°), \quad where\ S_{ref} = L_{LGL} D_{LGL}$$

In contrast, additional CFD analyses were conducted for the landing gear foot. The landing gear foot has 0° of the α_{inc}. Its AR has a value generally between 20 and 30 where a higher drag coefficient is reported [13]. Figure 7 shows a variation of the drag coefficient of a cylinder with 23 of AR. The reference geometry information for the calculation is as follows: $D_{rod} = 15\ mm, and\ L_{rod} = 350\ mm$. As can be seen, the drag coefficient is much higher than that of a cylinder with 10 of AR when the θ_{pitch} has a high value. For the drag model, regression functions are derived based on the CFD analysis results.

$$(5) \quad C_{D_{LGF}} = f(\theta_{pitch}), \ where\ S_{ref} = L_{LGF} D_{LGF}$$

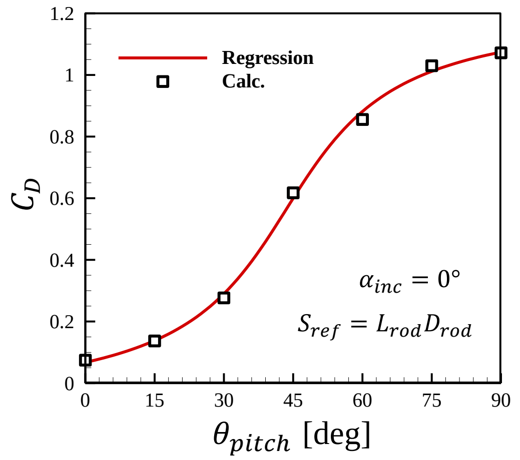

Figure 7: Drag coefficient variation of a cylinder with 23 of AR

Presented at 45th European Rotorcraft Forum, Warsaw, Poland, 17-20 September, 2019

2.6. Interference effect

Because the components of the radial layout are the supporting rods, the centre plate, and the T-shape landing gear, the sum of the components' EPDA in Eq. (1) is expressed as below.

(6) $\sum f_{component} = \sum f_{rod} + f_{centre} + f_{LGL} + f_{LGF}$

By the regression equations obtained above, each EPDA can be calculated fast. The remaining is the κ_{inf} in Eq. (1) for consideration of interference effect between the components. In order to derive this factor, CFD analysis results of a whole body are compared with the sum of the components' EPDA. In this study, the κ_{inf} is defined as Eq. (7), which is a ratio of the two calculated drag force.

(7) $\kappa_{inf} \equiv \dfrac{Drag\ by\ CFD}{Drag\ by\ sum} = \dfrac{f_{whole}}{\sum f_{component}}$

A reference 3D model of a quadrotor and hexarotor configuration was set respectively for calculating the numerator of the κ_{inf}. The denominator is obtained by the regression equations. The calculation results are tabulated in Table 2-a, 2-b, and the trend of the κ_{inf} is displayed in Figure 8. The κ_{inf} has values under 1, which means the interference effect decreases the drag force compared to that of an isolated condition. As the θ_{pitch} increases the κ_{inf} tends to increase, which implies that the interference effect is reduced. The κ_{inf} has the maximum value at $\theta_{pitch} = 90°$, which means the minimum interference effect. This phenomenon mainly results from the interference between the cylindrical tubes. When two cylinders are placed in abreast or staggered position, the drag coefficient of the downstream cylinder significantly decreases [15]. Although the κ_{inf} is lower than 1 in both configuration, the trend of the κ_{inf} is slightly different to each other. The κ_{inf} of the quadrotor remains nearly constant at approximately 0.94 after 30° of the θ_{pitch}, which means the interference effect almost disappears. This result corresponds with the reference [15]. In contrast, the κ_{inf} of the hexarotor keeps having lower value compared to the quadrotor case. This distinction might result from the different configuration (the number of rotors). One set of additional supporting rods in the middle of the body frame keeps causing the interference effect on the landing gear. For the drag model, regression functions for the κ_{inf} are derived based on the CFD analysis results.

(8) $\kappa_{inf} = f(\theta_{pitch},\ N_{rotor})$

(9) $f_{frame} = \kappa_{inf} \sum f_{component}$

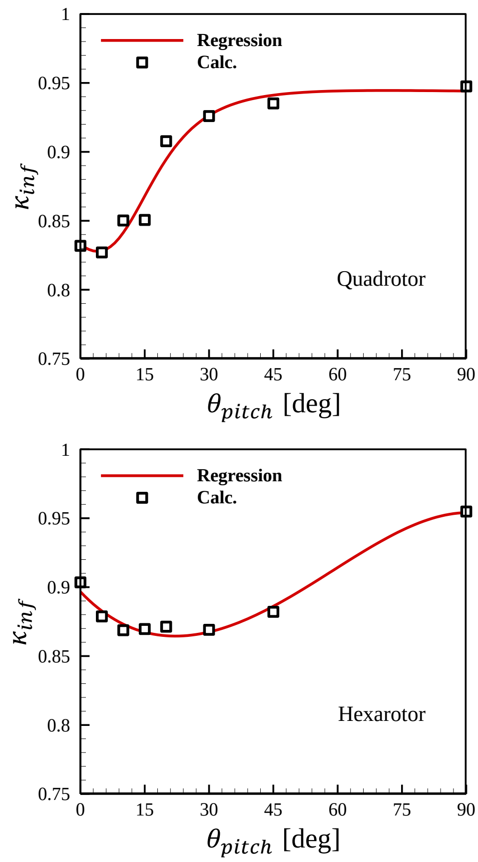

Figure 8: Interference factor variation

Table 2-a: Calculation condition and results of quadrotor

Geometry [mm]		V_∞	θ_{pitch} [deg]	Drag Sum [N]	Drag CFD [N]	κ_{inf}
D_{rod}	10	15	5	1.053	0.871	0.83
L_{rod}	150					
D_{centre}	150		10	1.226	1.043	0.85
h_{centre}	14					
D_{LGL}	10		20	1.712	1.554	0.91
L_{LGL}	150					
D_{LGF}	10		90	3.956	3.748	0.95
L_{LGF}	200					

Table 2-b: Calculation condition and results of hexarotor

Geometry [mm]		V_∞	θ_{pitch} [deg]	Drag Sum [N]	Drag CFD [N]	κ_{inf}
D_{rod}	25	15	5	5.003	4.397	0.88
L_{rod}	300					
D_{centre}	200		10	5.389	4.664	0.88
h_{centre}	29					
D_{LGL}	25		20	6.512	5.674	0.87
L_{LGL}	300					
D_{LGF}	25		90	12.18	11.63	0.95
L_{LGF}	400					

2.7. Additional attachment (Payload)

Drag by a payload should be separately given by a user because of two reasons. First, this model aims to reflect influence of a geometric difference of the multirotor frame in conceptual design phase. Second, payloads of the multirotors do not have standardized shape and dimension, which makes hard to do modelling them appropriately. Likewise, it is practically difficult to consider the interference effect between the body frame and payloads. Therefore, EPDA of a payload is another input parameter.

2.8. Estimation flow of the Drag model

Through a series of processes presented in Figure 9, the drag force induced by the body frame at forward flight can be calculated. The EPDA of the each component is calculated by the geometric input parameters (Eq. (2) – Eq. (5)). Using the κ_{inf} determined by the θ_{pitch}, the EPDA of the entire body frame is obtained (Eq. (6) – Eq. (8)). With EPDA of a payload added, the drag force is calculated by multiplying dynamic pressure to the total EPDA (Eq. (9)).

(9) $$Drag = \frac{1}{2}\rho V_\infty^2 f_{total}, \quad where$$
$$f_{total} = f_{frame} + f_{payload},$$
$$f_{frame} = \kappa_{inf}(\sum f_{rod} + f_{centre} + f_{LGL} + f_{LGF})$$

2.9. Validation of the drag model

Since the presented model estimates the drag force induced only from the body frame, it is difficult to find appropriate data for the validation from public domain. Hence, the developed drag model is validated by comparing CFD analysis results for 3D models that have another dimension. The validation results are shown in Figure 10. The detailed information are tabulated in Table 3-a, and 3-b, each for the quadrotor and the hexarotor.

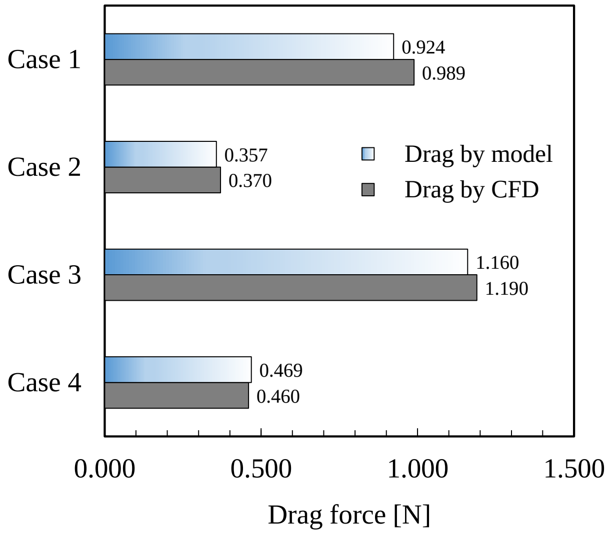

Figure 10: Drag model validation

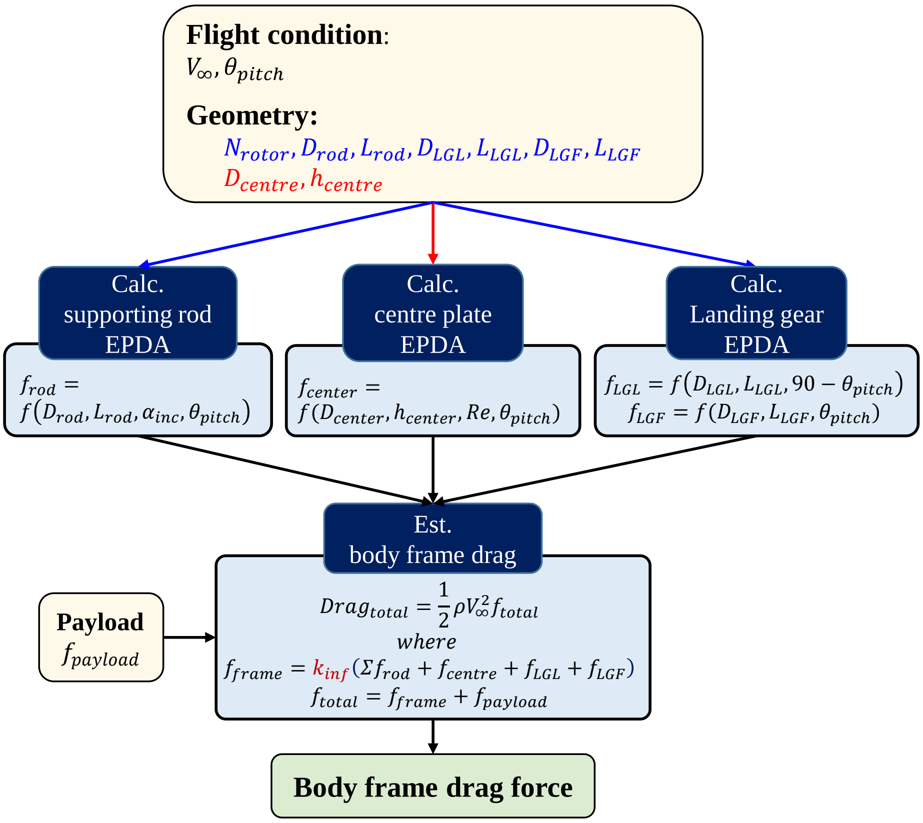

Figure 9: Calculation process for body frame drag

Presented at 45th European Rotorcraft Forum, Warsaw, Poland, 17-20 September, 2019

Table 3-a: Validation case and results of quadrotor

Geometry [mm]			V_∞	θ_{pitch} [deg]	Drag model [N]	Drag CFD [N]	Err. [%]
D_{rod}	15	Case 1	15	5	0.924	0.989	-6.6
L_{rod}	120						
D_{centre}	100						
h_{centre}	19						
D_{LGL}	15	Case 2	9	8	0.357	0.370	-3.1
L_{LGL}	120						
D_{LGF}	15						
L_{LGF}	133						

Table 3-b: Validation case and results of hexarotor

Geometry [mm]			V_∞	θ_{pitch} [deg]	Drag model [N]	Drag CFD [N]	Err. [%]
D_{rod}	10	Case 3	15	10	1.160	1.190	-2.5
L_{rod}	150						
D_{centre}	150						
h_{centre}	14						
D_{LGL}	10	Case 4	10	5	0.469	0.460	2.0
L_{LGL}	150						
D_{LGF}	10						
L_{LGF}	200						

The developed drag model shows high accuracy comparable to CFD analysis. The averaged absolute error is 3.55 % in four cases. While achieving the accuracy, the calculation time required to obtain drag force is reduced significantly from 15 hours in CFD to a few seconds in the model on average. Thus, this model can be applied appropriately in the conceptual design phase where numerous calculations are required and short calculation time is desirable.

Although the developed drag model shows satisfactory analysis results in terms of calculation time and accuracy compared to CFD analysis, there exist a few limitations in this model caused by the assumptions.

1) The geometric layout is limited to a quadrotor and hexarotor that has the radial layout with the T-shape landing gear. Another configuration such as an octarotor can be estimated when κ_{inf} is obtained by the presented method in Chapter 2.6.
2) The data used in deriving the regression equations are based on the restricted range of Reynolds number and AR of the components. The Reynolds number region is subcritical region under approximately 500,000. Thus, the developed drag model does not guarantee the result under conditions outside the Reynolds number and AR range.
3) Although the additional drag for an external payload can be added by a form of EPDA, the interference between the payload and the body frame is not considered currently.
4) This model is not for a dynamics analysis. This model is applicable to steady or quasi-steady flight conditions.

Despite these limitations, for the radial-layout quad and hexarotor, the developed drag model makes it possible to consider the drag force of the body frame according to geometric variation in the conceptual design phase.

3. APPLICATION OF DRAG MODEL

In Chapter 3, a design optimization example is presented. The developed drag model is embedded in a conceptual design optimization framework for the multirotors, CLOUDS [2]. CLOUDS is able to conduct a mission-oriented design optimization suggesting an optimal combination of a rotor, a motor, an Electric Speed Controller (ESC), and a battery. It consists of multidisciplinary analysis modules including attitude, aerodynamics, and electric propulsion system analysis. Among them, the developed drag model is applied in the attitude module. The overall design flow of CLOUDS is displayed in Figure 11. The detailed description about CLOUDS can be found in Reference [2].

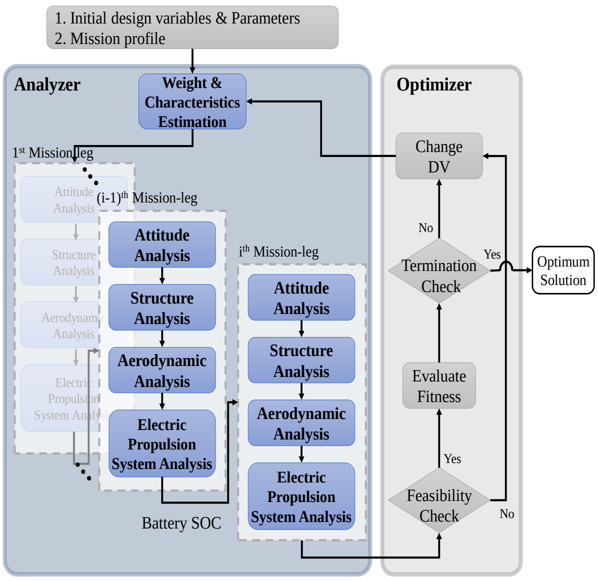

Figure 11: Overall design procedure of CLOUDS [2]

Presented at 45th European Rotorcraft Forum, Warsaw, Poland, 17-20 September, 2019

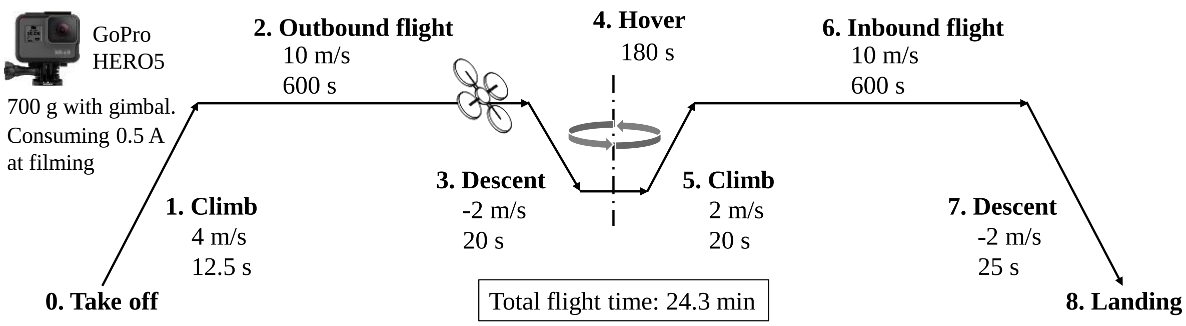

Figure 12: Fliming mission profile

3.1. Optimization outline

3.1.1. Design variables

Two multirotors are designed according to whether the drag model is applied or not. Design variables designated in the optimization are related with the main components of the multirotors such as a rotor, a motor and a battery. The design variables set are tabulated in Table 4.

Table 4: Design variables

Component	Design variables	
Rotor	D_{rotor} [in]	Rotor diameter
	p_{rotor} [in]	Rotor pitch
Motor	K_v	Motor speed constant
Battery	N_{cell}	The number of cells
	Capacity [Ah]	Battery total capacity
ESC	A_{max} [A]	Max. allowable current
Supporting rod	D_{rod} [mm]	Rod diameter
	L_{rod} [mm]	Rod length

Among the 8 input parameters concerning the body frame shown in Figure 3, there is a little difficulty in determining values for them except for D_{rod} and L_{rod} in the optimization process. In order to handle this problem, 6 parameters are determined by a correlation with the 2 parameters: D_{rod}, and L_{rod}. The relations are listed as follow.

$$D_{centre} = 0.65D_{rotor}$$
$$h_{centre} = 1.4D_{rod}$$
$$D_{LGL} = D_{rod}$$
$$L_{LGL} = 0.818L_{rod}$$
$$D_{LGF} = 0.6D_{rod}$$
$$L_{LGF} = 1.646D_{rotor}$$

The numbers multiplied in the right hand side are obtained by investigating the commercially available frame kits: Tarot FY650, DJI S800, DJI S900, and ARRIS M1050.

3.1.2. Misson profile and objectives

Mission profile in this example is a generic mission of filming multirotors. The mission profile, shown in Figure 12, consists of 7 mission legs and total flight time is 24.3 minutes.
The objective of the optimization is minimizing a total weight and remaining battery capacity after completing the mission. The constraints are set about motor throttle for control margin. Some parameter associated with the rotor and the battery is taken from Reference [2].

The optimization method used is NSGA-Ⅱ [16], one of the global optimization schemes, because the design space shows highly nonlinear characteristics [2]. The design space is presented in Table 5. The upper and lower boundary value of each design variable is determined based on commercially available components of the multirotors. The EPDA of GoPro is given as an input. The optimization problem can be summarized as follows.

- Objective:
  Minimize total weight with 0.7 kg payload
  Minimize a remaining battery capacity
- Constraint:
  Under 65 % of motor throttle at hover
  Under 80 % of motor throttle at inbound flight
- Optimization scheme:
  NSGA-Ⅱ

Table 5: Design space

		Upper	Lower
D_{rotor}	[in]	7	30
p_{rotor}	[in]	3	10
K_v		100	1000
N_{cell}		2	12
Capacity	[Ah]	1	20
A_{max}	[A]	10	60
D_{rod}	[mm]	10	30
L_{rod}	[mm]	100	500

Presented at 45th European Rotorcraft Forum, Warsaw, Poland, 17-20 September, 2019

3.2. Optimization results

After approximately 7,000 iterative calculations, an optimal component combination of the two vehicle is obtained respectively. Vehicle1 is the case where the developed drag model is applied, and Vehicle 2 is the case where a constant drag value is given. Constant value of 1.1 is given for a drag coefficient of Vehicle 2. The optimal values of the design variables are tabulated in Table 6. As can be seen, a rotor-motor-battery set is different to each other. This result might be caused from the drag model since all analysis methods are the same except for the drag force calculation.

Table 6: Optimal design variables

		Vehicle 1 (Drag model)	Vehicle 2 (Constant $C_D = 1.1$)
D_{rotor}	[in]	16	13
p_{rotor}	[in]	3	2
K_v		360	370
N_{cell}		6	10
Capacity	[Ah]	12.62	9.52
A_{max}	[A]	36	30
D_{rod}	[mm]	10	10
L_{rod}	[mm]	230	192

3.2.1. Dimension and weight

Using a top-view schematics diagram, the overall dimension of the optimized multirotors is displayed in Figure 13 on the same scale. For simplicity, the landing gear is erased in the schematics diagram. Because of the bigger rotor and longer rod length in Vehicle 1, overall dimension is larger than that of Vehicle 2.

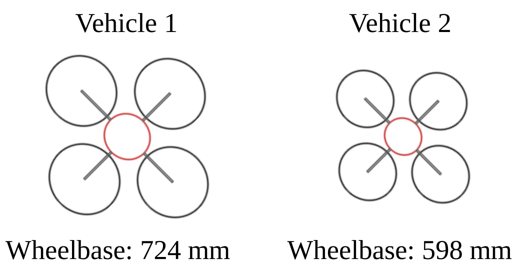

Figure 13: Schematics of the designed multirotors

The weight information of the designed multirotors is shown in Figure 14. Equations for the weight estimation are summarized in Appendix 1 and the description about them can be found in Reference [2]. The weight of the avionics indicating a flight control computer is given as 50 g. The weight of the additional includes GPS and communication system that is also given as 91.6 g. The weight of rotors, motors and ESCs indicates the all-up weight by multiplying the number of rotors to a single weight. Even though Vehicle 1 has a larger dimension and rotor diameter, the total weight of Vehicle 1 is 200 g lower than that of Vehicle 2. Among the component weights, the battery weight makes major difference between two vehicles. The heavier battery in Vehicle 2 results in heavier total weight despite the lighter single components.

Table 7: Single component weight & Total weight

Component Weigth [g]	Vehicle 1	Vehicle 2
Single rotor	27.88	16.69
Single motor	286.73	277.82
Single ESC	39.95	32.96
Total weight	5187.25	5383.31

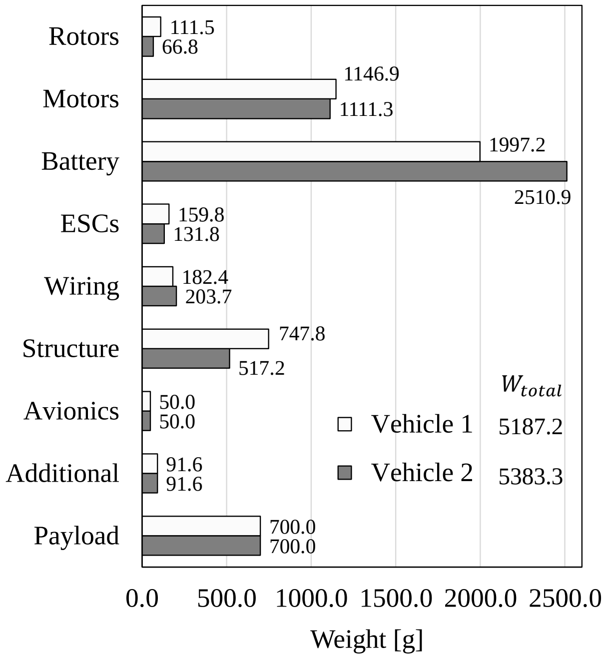

Figure 14: Weight information by the components

3.2.2. Performance

The performance parameters of the optimal multirotors while carrying out the mission are presented in Table 8-a, and 8-b. First, the θ_{pitch} and drag force by the frame in the forward flight is different to each other. Since the drag model is applied to Vehicle 1, the drag force incurred from the body frame is estimated by geomtric information. In Vehicle 2, the given constant drag coefficient is used. When a reference area is defined as sum of components' frontal area (cylinders, circular plate, and payload), the drag coefficient of the overall multirotor can be calculated as follow.

Presented at 45th European Rotorcraft Forum, Warsaw, Poland, 17-20 September, 2019

Vehicle 1	Climb	$C_D = 0.979$	$S_{ref} = 0.0793\,m^2$
	Forward	$C_D = 0.289$	
Vehicle 2	Climb	$C_D = 1.100$	$S_{ref} = 0.0614\,m^2$
	Forward	$C_D = 1.100$	

The drag coefficient of Vehicle 1 is calculated by the drag model depending on the flight condision. The given constant drag coefficient for Vehicle 2 is much higher compared to the drag coefficient of Vehicle 1 especially in the forward flight. The larger drag coefficient of Vehicle 2 requires as possible as the reduced dimension to obtain smaller drag force in the forward flight. The dimension of a multirotor depends on the rotor diameter, so that Vehicle 2 has smaller rotor diameter.

The smaller rotor induces higher mechanical power and electric power in the same flight condition (Table 8-a and 8-b). That means a battery with the larger energy is eventually required. The energy of the battery in each designed multirotor is calculated as follows: 280 Wh in Vehicel 1, and 352 Wh in Vehicle 2.

Table 8-a: Performance of the vehicle 1 (Drag model)

Mission leg #	θ_{pitch} [deg]	Ω_{rotor} [RPM]	P_{mech} [W]	P_{elec} [W]	η_m [%]	I_d [A]
1	0	5116	116.2	137.9	84.28	22.18
2	1.6	3658	121.5	146.1	83.19	24.91
3	0	4425	110.4	131.3	84.11	23.12
4	0	4603	111.6	132.5	84.18	23.52
5	0	4842	112.9	134.1	84.20	23.98
6	1.6	3658	121.5	146.0	83.24	26.64
7	0	4423	110.4	131.2	84.11	24.34
Drag force at the forward flight: 1.40 N						

Table 8-b: Performance of the vehicle 2 (Constant C_D)

Mission leg #	θ_{pitch} [deg]	Ω_{rotor} [RPM]	P_{mech} [W]	P_{elec} [W]	η_m [%]	I_d [A]
1	0	7806	152.4	180.0	84.65	17.38
2	10.9	5850	153.2	179.0	85.58	18.30
3	0	6891	141.4	166.9	84.74	17.62
4	0	7141	143.6	169.6	84.68	18.06
5	0	7423	146.2	172.8	84.60	18.55
6	10.9	5850	153.2	179.0	85.58	19.58
7	0	6887	141.3	166.8	84.73	18.45
Drag force at the forward flight: 4.13 N						

Among various performance parameters, a drive current and motor efficiency is plotted by the mission leg in Figure 15. The drive current is obtained by summing all motor current (Eq.(9)).

$$(9)\quad I_d = \sum_{n=1}^{N_{rotor}} I_{m_n}$$

When seeing the motor efficieny, the optimal combination of the two multirotors has comparable efficiency except for the forward flight. On the other hand, in the forward flight the discrepancy of the motor efficiency gets larger. This is because that the drag force causes a shift of the operating condition. In Vehicle 1, the variation of mechanical power in the first two leg (Climb and forward flight) is relatively larger, showing 10 % of variation from 116.4 W to 121.5 W. In contrast, the variation of mechanical power of Vehicle 2 during the same mission leg is negligible from 152.4 W to 153.2 W because of the same drag coefficient regardless of the flight condition.

Similarly, the variation of the drive current is much severe in Vehicle 1. Since the drive current determined the required capacity of the battery, the prediction of the drive current is essential. As can be seen, the variation of the drive current is affected by the drag force, the drag force plays the important role in the design process.

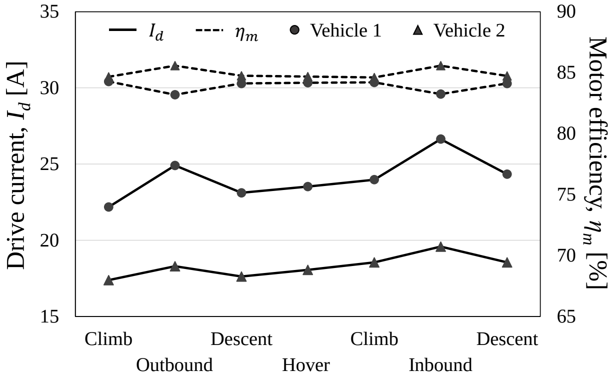

Figure 15: Drive current and motor efficiency

4. CONCLUSION

In this paper developed is the practical drag estimation model for the multirotor configuration for the purpose of the application to the conceptual design phase. In order to apply the drag model in design process, the model are based on some assumptions about a geometric layout and flight status: a radial layout and steady flight status. Furthermore, the components of multirotors' frame are modelled as the simple solid figures: cylindrical tube and circular plate. By using CFD analyses, drag coefficient of each component and interference factor are obtained. Then, the regression equations are derived for rapid calculation in the conceptual design phase. Through this drag model, the geometric variation of the multirotors can be considered in the design process.

Presented at 45th European Rotorcraft Forum, Warsaw, Poland, 17-20 September, 2019

After embedding the drag model in the conceptual design optimization framework, the optimization results for the generic mission profile are presented as an example. In the optimization example, the different multirotors are designed depending on the drag coefficient. The drag force incurred by the body frame has effect on the performance variation of the multirotors, eventually resulting in the different components combination of the optimized multirotors. As a next step for drag estimation for a complete multirotor, a few things should be modelled and added such as external attachments, rotor wake effect, and horizontal force of the rotor in forward flight.

.

ACKNOWLEDGEMENT

This research was supported by Unmanned Vehicles Advanced Core Technology Research and Development Program through the National Research Foundation of Korea (NRF), Unmanned Vehicle Advanced Research Centre (UVARC) funded by the Ministry of Science and ICT, the Republic of Korea (NRF-2016M1B3A1A03937680).

REFERENCES

[1] Cai, G., Dias, J. and Seneviratne, L., "A survey of small-scale unmanned aerial vehicles: Recent advances and future development trends," *Unmanned Systems*, Vol.2, No.2, 2014, pp.175-199.

[2] Lim, D., Kim, H., Lee, B. and Yee, K., "Unified framework for analysis and design optimization of a multirotor unmanned aerial vehicle," 44th European Rotorcraft Forum, Delft, Netherlands, Sep. 2018.

[3] Bershadsky, D., Haviland, S., and Johnson E.N., "*Electric* multirotor propulsion system sizing for performance prediction and design optimization," AIAA SciTech 2016, AIAA, San Diego, CA, Jan. 2016.

[4] Winslow, J., Hrishikeshavan, V., and Chopra, I., "Design methodology for small scale unmanned quadrotors," 55th AIAA Aerospace Sciences Meeting, Grapevine, TX, Jan. 2017.

[5] Gatti, M., Giulietti, F. and Turci, M., "Maximum endurance for battery-powered rotary-wing aircraft," Aerospace *Science and Technology*, 45, 2015, pp.174-179.

[6] Hwang, M., Cha, H., and Jung, S., "Practical Endurance Estimation for Minimizing Energy Consumption of Multirotor Unmanned Aerial Vehicles," *Energies*, Vol. 11, No. 9, Aug. 2018.

[7] Dongjie S., Xunhua D., Xiaowei Z., and Quan Q., "A Practical Performance Evaluation Method for Electric Multicopters," *IEEE/ASME Transactions on Mechatronics*, Vol. 22, No. 3, June 2017.

[8] Müller, M., eCalc: the most reliable RC calculator on the web. URL: http://www.ecalc.ch/indexcalc. htm [Cited 15 June 2015].

[9] Williams, J. E., and Vukelich, S. R., "The USAF Stability and Control Digital DATCOM. Volume ii. Implementation of DATCOM methods," MCDONNELL DOUGLAS ASTRONAUTICS CO ST LOUIS MO, Apr. 1979.

[10] F. R. Menter, "Two-Equation Eddy-Viscosity Turbulence Models for Engineering Application," *AIAA Journal*, Vol. 32, No. 8, Aug. 1994, pp. 1598-1605.

[11] P. E. Smirnov and F. R. Menter, "Sensitization of the SST Turbulence Model to Rotation and Curvature by Applying the Spalart-Shur Correction Term," *ASME Paper GT 2008-50480*, Berlin, Germany. 2008.

[12] Nian-Sheng C., "Calculation of Drag Coefficient for Arrays of Emergent Circular Cylinders with Pseudofluid Model," *Journal of Hydraulic Engineering*, Vol. 139, No. 6, June, 2013, pp. 602-611.

[13] Zdravkovich, M. M., Brand, V. P., Mathew, G., and Weston, A., "Flow Past Short Circular Cylinders with Two Free Ends," *Journal of fluid mechanics*, Vol. 203, Jun. 1989, pp. 557-575.

[14] Hoerner S., *Fluid-dynamic drag; practical information on aerodynamic drag and hydrodynamic resistance*, 2nd edition, Midland Park, NJ, 1958.

[15] Sumner, D., "Two circular cylinders in cross-flow: a review," *Journal of fluids and structures*, Vol. 26, No. 6, Jul. 2010, pp.849-899.

[16] Deb, K., Agrawal, S., Pratap, A., and Meyarivan, T., "A Fast and Elitist Multi-Objective Genetic Algorithm: NSGA-II," IEEE Transactions on Evolutionary Computation, Vol. 6, No. 2, 2002, pp. 182-197

APPENDIX

1) WEIGHT ESTIMATION EQUATIONS

Rotor [2]	$W_R = \{p_1(D_{rotor})^2 + p_2 D_{rotor} + p_3\}N_b$ $p_1 = 0.0913, p_2 = -0.783, p_3 = 3.098$
Motor [2]	$W_m = 252{,}538(K_v)^{-1.152}$
Battery [3]	$W_B = (p_1 N_{cell} + p_2)Capacity$ $p_1 = 0.02637, p_2 = 2.04 * 10^{-5}$
ESC [2]	$W_{ESC} = 1.1652A_{max} - 2$
Wiring [3]	5 % of propulsion system
Frame [2]	$W_{Frame} = 1.79(W_{center} + W_{rod} + W_{LG})$